Platinum-Nickel Alloy Nanowire Electrocatalysts Transform into Pt-Skin Beads-on-Nanowires Keeping Oxygen Reduction Reaction Activity During Potential Cycling

Yu Zhuang,[1] Yoshimi Iguchi,[1] Tianchi Li,[1] Masaru Kato,[1,2] Yasir Arafat Hutapea,[3] Akari Hayashi,[3] Takeshi Watanabe,[4] and Ichizo Yagi[1,2]**

[1] Graduate School of Environmental Science, Hokkaido University, N10W5, Kita-ku, Sapporo 060-0810, Japan

[2] Faculty of Environmental Earth Science, Hokkaido University, N10W5, Kita-ku, Sapporo 060-0810, Japan

[3] Platform for Inter/Transdisciplinary Energy Research, Kyushu University, 744 Motooka, Nishi-ku, Fukuoka 819-0395, Japan

[4] Industrial Application Division, Japan Synchrotron Radiation Research Institute, Sayo, Hyogo 679-5198, Japan.

*Corresponding authors: masaru.kato@ees.hokudai.ac.jp (MK); iyagi@ees.hokudai.ac.jp (IY).

KEYWORDS. Alloy nanowires, oxygen reduction reaction, polymer electrolyte fuel cell, Pt skin, beads-on-nanowires, Ostwald ripening, nanomaterials electrocatalysts, X-ray absorption spectroscopy.

ABSTRACT: We synthesized PtNi alloy nanowires (PtNi NWs) at three different temperatures of 433, 493 and 533 K (NW_{433K}, NW_{493K} and NW_{533K}, respectively), and then investigated their catalytic activity and durability for the oxygen reduction reaction (ORR) in acidic media. Ni contents in the PtNi NWs increase as the synthesis temperatures increase from below 5 at. % for NW_{433K} up to about 15 at. % for NW_{493K} and NW_{553K}. PtNi nanoparticles (PtNi NPs), which are the unconsumed intermediate during the NW growth, also coexist for NW_{433K} and NW_{493K} but not for NW_{533K}. NW_{493K} and NW_{533K} show similar initial activity for the ORR but higher than NW_{433K}, suggesting that higher Ni contents are critical to achieving higher initial ORR activity. Accelerated durability tests (ADTs) show that NW_{493K} is the most durable, suggesting that the co-presence of PtNi NPs is critical to durability. Only NW_{493K}, with a high Ni content of 15 at. % and coexisting PtNi NPs, gave better results in both cases. Scanning transmission electron microscopy and energy dispersive X-ray spectroscopy of PtNi NWs reveal a structural transformation of NW_{493K} into Pt-skin beads-on-nanowires, involving the Ostwald ripening of coexisting PtNi NPs. This structural transformation is coupled with changes in surface composition and surface electronic structure, as confirmed by CO stripping voltammogram and *in situ* X-ray absorption spectroscopy, resulting in high durability and suppression of Pt and Ni dissolution. Understanding such structural transformation during potential cycling will help us to design and develop highly active and durable Pt-based electrocatalysts.

INTRODUCTION

Polymer electrolyte fuel cells (PEFCs) are considered to be a high energy conversion efficiency device to supply electricity and heat with low environmental impact by using hydrogen.[1] The sluggish chemical kinetics of the oxygen reduction reaction (ORR) at the cathode limits the performance of PEFCs.[1] Pt is the most active ORR catalyst among all metals and therefore has been widely used as ORR catalyst in PEFCs. Since the ORR activity of Pt is unsatisfactory and the cathode requires a large amount of Pt, highly active and durable Pt or Pt alloy electrocatalysts should be developed even under harsh reaction conditions of PEFCs.

Alloying Pt with a second metal such as Ni [2–6] changes the densities of the surface electronic states of Pt and then enhances the catalytic activity of ORR. Shape-controlling of Pt alloy catalysts has also been investigated due to their high initial activity.[2,7–14] In particular, ultrathin Pt-Ni alloy nanowires (PtNi NWs) as one-dimensional nanomaterials have larger contact areas with carbon supports and can, in principle, suppress metal dissolution, migration, and aggregation, compared withNPs.[7,9,10,14,15] There is a challenge of developing highly durable PtNi NWs with high nickel contents even during potential cycles. Pt_3Ni single crystalline electrodes are already reported to show high ORR activity[5,16] and PtNi NWs with an atomic ratio of Pt:Ni =3:1 can be expected to show high ORR activity as well. Although PtNi NWs can be synthesized with high Ni contents such as 48 at% of Ni, Ni can be easily reached out during several potential cycles and down to about 6 at% of Ni.[3] The formation of the Pt-skin on nanostructured Pt alloy catalysts is often mentioned as an effective way to prevent etching of alloying components including Ni[17–19] and provides higher catalytic performance by significantly lowering the binding energies of ORR intermediates (O, OH and OOH). [20–24] Interestingly, during potential cycles, the structure of PtNi nanowires can be converted to a branched nanostructure involving the Ostwald ripening supported

by the coexisting PtNi NPs.[3] Similar branched or waved nanostructures have also been reported.[19,25–27] These results encourage us to synthesize PtNi NWs with different Ni contents and understand the relationship between the activity, durability, Ni contents and structural changes via Ostwald ripening during potential cycles.

Herein, we report preparation of PtNi NWs at three different synthesis temperatures of 433, 493 and 553 K to obtain PtNi NWs with different Ni contents in the presence and absence of PtNi NPs, their ORR electrocatalytic activity and durability. During accelerated durability tests (ADTs), a self-motivated structural transformation of PtNi NWs into Pt-skin beads-on-nanowires was observed for one type of PtNi NWs with the copresence of PtNi NPs. The relationship of Pt:Ni ratios and co-existing PtNi NPs with the shape, surface structure and electronic state is discussed based on results of scanning transmission electron microscopy (STEM), inductively coupled plasma mass spectrometry (ICP-MS), CO stripping voltammetry, and X-ray absorption spectroscopy (XAS) of the PtNi NWs.

RESULTTS AND DISCUSSION

PtNi NWs were synthesized from metal sources of $[Pt(acac)_2]$ (acac = acetylacetonato) and $[Ni(acac)_2]$ in oleylamine containing $[Mo(CO)_6]$, cetyltrimethylammonium chloride (CTAC), and glucose at three different synthesis temperatures under Ar for 2 h: 433, 493, and 553 K and denoted as NW_{433K}, NW_{493K} and NW_{553K}, respectively. The obtained PtNi NWs were supported on Vulcan XC-72R carbon black (NW_{433K}/C, NW_{493K}/C and NW_{553K}/C). An electrode was prepared by drop-casting and drying catalyst ink with Nafion on the surface of a glassy carbon (GC) disk and then used as a rotating disk electrode. STEM and high angle annular dark-field (HAADF)-STEM observation of all the three products revealed that PtNi NWs have an average diameter of ca. 2.0

nm (**Figure 1**). The averaged NW length depends on the synthesis temperature and increases with higher synthesis temperature: averaged 31 nm for NW_{433K}, averaged 56 nm for NW_{493K} and averaged 78 nm for NW_{553K} (**Figure S1** in Supporting Information). Note that PtNi NPs were present with PtNi NWs in HAADF-STEM images (**Figure 1a** and **1b**) whereas almost no NP was found (**Figure 1c**). These PtNi NPs were synthesized as the intermediate together with PtNi NWs and tended to decrease with increasing synthetic temperatures. Because PtNi NWs were grown by the oriented attachment mechanism on PtNi NPs, and higher synthetic temperatures help Ostwald ripening, resulting in decrease of the coexisting PtNi NPs.[2,3,12,28–30]

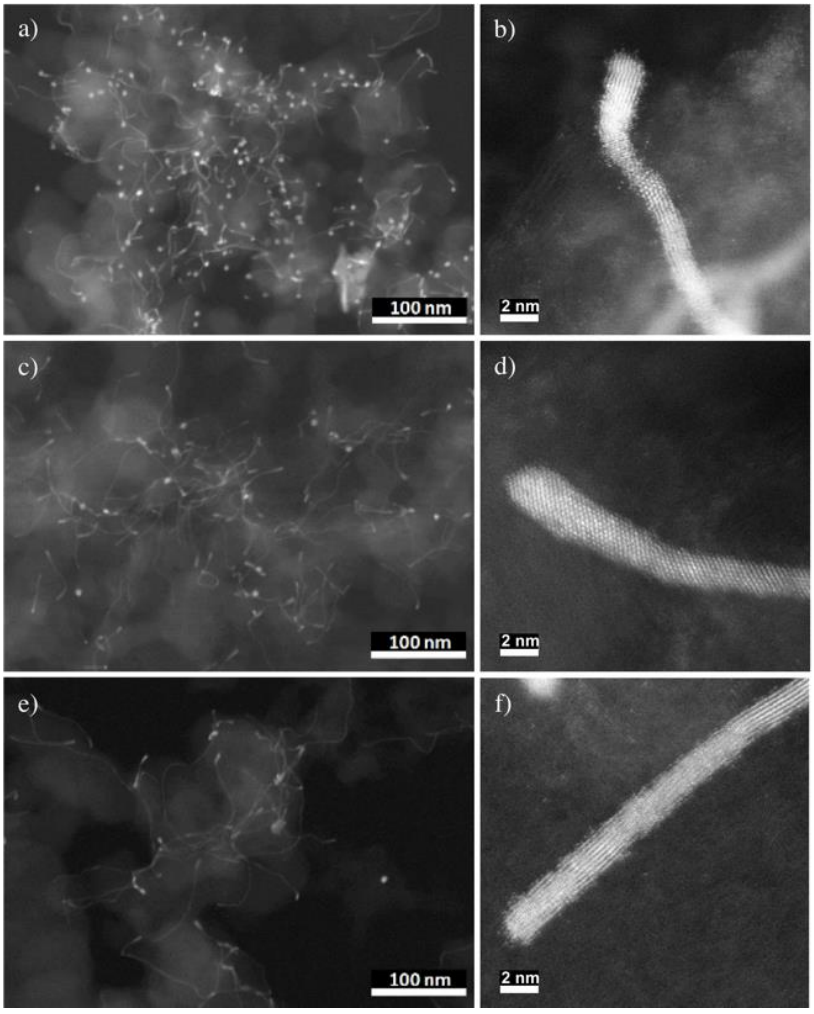

Figure 1. HAADF-STEM images of (a,b) NW_{433K}/C (c,d) NW_{493K}/C, (e,f) NW_{553K}/C.

Powder X-ray diffraction (XRD) patterns of PtNi NWs show characteristic 111 diffraction lines of the fcc structure (**Figure S2**). The peak position for NW_{493K} and NW_{553K} was clearly shifted to higher angles than that of commercially available Pt/C as the standard sample, and the peak-top position for NW_{433K} was not shifted as high as the others. Atomic percentages of Pt in each type of PtNi NW can be calculated from the peak-top positions using Vegard's law[31] to be 95.5, 90.1 and 88.3 at% for NW_{433K}/C, NW_{493K}/C and NW_{553K}/C, respectively, which are similar to those determined by ICP-MS (**Table S1**). Thus, NW_{493K} and NW_{553K} have higher Ni contents than NW_{433K}.

PtNi NWs in NW_{493K} and NW_{553K} remain PtNi alloy but those in NW_{433K} do not after electrochemical cleaning, confirmed by both ICP-MS and STEM-energy dispersive spectroscopy (STEM-EDS). The electrochemical cleaning as a pretreatment of the catalysts was performed in a 0.1 M $HClO_4$ solution under Ar for 100 potential cycles at 100 mV s^{-1} between +0.10 and +1.00 V vs. RHE. Metal compositions were determined to be $Pt_{94}Ni_6$ for NW_{433K}, $Pt_{86}Ni_{14}$ for NW_{493K} and $Pt_{84}Ni_{16}$ for NW_{553K}. Unalloyed Ni was leached out for NW_{433K}. STEM-EDS mapping (**Figure S3**) also shows that Ni is uniformly distributed in PtNi NWs. This result suggests that the synthesis temperature contributes to keeping the Ni contents in PtNi NWs even after the electrochemical cleaning process. In other words, PtNi NW_{493K} and NW_{553K} were well alloyed while NW_{433K} was not so much, which is in good agreement with the XRD results (**Figure S2**).

Hydrodynamic voltammetry of NW_{433K}/C, NW_{493K}/C, and NW_{553K}/C after the electrochemical cleaning process was taken in a 0.1 M $HClO_4$ aqueous solution under oxygen to understand the electrocatalytic ORR activity. Linear sweep voltammograms (LSVs) of them showed reduction currents under oxygen (**Figure 2**) but not under Ar (**Figure S4**), indicating that the PtNi NWs

catalysts show the electrocatalytic ORR activity was determined. The initial mass activities (MAs) and specific activities (SAs) at 0.9 V vs. RHE based on electrochemically active surface area determined by the Faradaic charge for the underpotentially deposited hydrogen ($ECSA_H$) were determined to be 0.16 A $(mg_{Pt})^{-1}$ and 3.0 A m^{-2} for NW_{433K}/C, 0.28 A $(mg_{Pt})^{-1}$ and 3.9 A m^{-2} for NW_{493K}/C, 0.28 A $(mg_{Pt})^{-1}$ and 2.5 A m^{-2} for NW_{553K}/C (**Table 1**). The MA and SA of Pt/C were 0.14 A $(mg_{Pt})^{-1}$ and 2.0 A m^{-2}, respectively. NW_{493K}/C and NW_{553K}/C showed almost the same initial MA and higher than NW_{433K}/C or Pt/C.

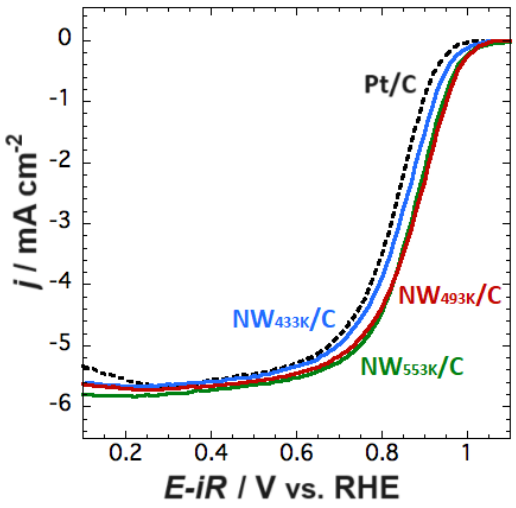

Figure 2. LSVs of NW_{433K}/C (The solid line in blue), NW_{493K}/C (The solid line in green), NW_{553K}/C (the solid line in red) and Pt/C (The dotted line in black). LSVs were recorded at 1600 rpm and 10 mV s^{-1} in a 0.1 M $HClO_4$ aqueous solution under oxygen. The Pt loading amount on the GC electrode was 12 μg cm^{-2}.

Table 1. Electrochemical results determined for NWs/C before and after the ADT.

	MA(A/mg_{Pt})	**SA_H(A/m^2)**	**$ECSA_H$(m^2/g_{Pt})**	**$ECSA_{CO}$(m^2/g_{Pt})**	**$ECSA_{CO}/ECSA_H$**
NW_{433K}/C	0.16	3.03	52	55	1.06
NW_{493K}/C	0.28	3.94	69	95	1.37

NW_{553K}/C	0.28	2.46	111	156	1.39
NW_{433K}/C_af	0.13	3.03	38	45	1.20
NW_{493K}/C_af	0.27	3.88	65	97	1.49
NW_{553K}/C_af	0.23	2.30	89	114	1.29

To understand the durability, LSVs (**Figure 3**) were recorded after 2000 square-wave potential cycles at 353 K stepping between the potentials at +0.6 V vs. RHE for 3 s and +0.9 V vs. RHE for 3s, in 0.1 M $HClO_4$ solution under Ar as the ADT, where the samples after the ADT show NW_{433K}/C_af, NW_{493K}/C_af and NW_{533K}/C_af. In typical Pt-based ORR electrocatalysts, the half-wave potential ($E_{1/2}$) after potential cycles is shifted to more negative than that of the initial $E_{1/2}$ due to loss of activity. Such $E_{1/2}$ shifts were observed after ADTs for NW_{433K}/C and NW_{553K}/C: $E_{1/2}$ shifted from 0.86 to 0.82 V vs. RHE for NW_{433K}/C and from 0.88 to 0.87 V vs. RHE (**Figure 3**). In contrast, NW_{493K}/C shows almost no change of $E_{1/2}$ at 0.88 V vs. RHE and it is the most durable in this work. The MA and SA of the most durable PtNi NW_{493K}/C_af, were determined to be 0.27 A $(mg_{Pt})^{-1}$ and 3.9 A m^{-2}, indicating that the electrocatalytic ORR activity had nearly no loss after the ADT. The MA and SA dropped down to 0.23 A $(mg_{Pt})^{-1}$ and 2.3 A m^{-2} for NW_{553K}/C_af and 0.13 A $(mg_{Pt})^{-1}$ and 3.0 A m^{-2} for NW_{433K}/C_af. All MAs, SAs and ECSAs before and after the ADT are summarized in **Table 1**.

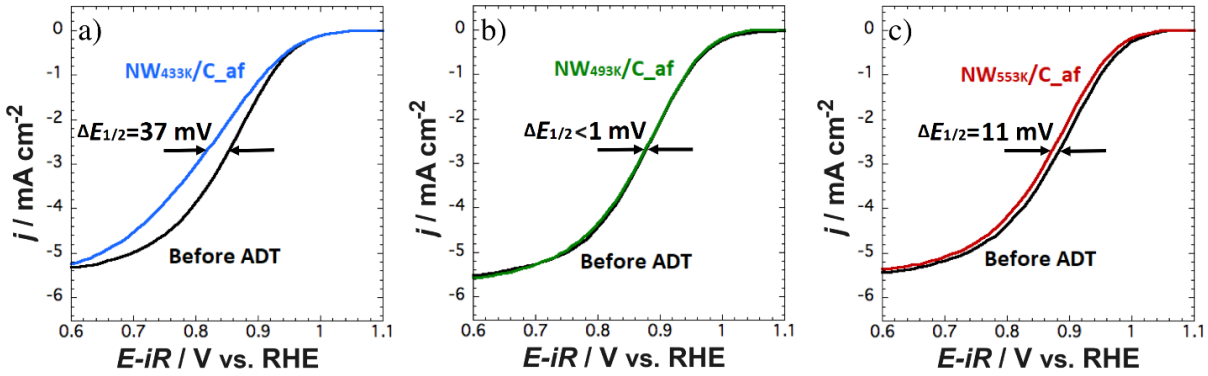

Figure 3. (a) LSVs of NW_{433K}/C before (in black) and after ADT (NW_{433K}/C_af in blue). (b) LSVs of NW_{433K}/C before (in black) and after ADT (NW_{493K}/C_af in green), (c) LSVs of NW_{553K}/C before (in black) and after ADT (NW_{553K}/C_af in red). LSVs were recorded at 1600 rpm and 10 mV s^{-1} in a 0.1 M $HClO_4$ aqueous solution under oxygen. The arrows indicate the $E_{1/2}$ difference ($\Delta E_{1/2}$) before and after ADT: 37 mV for NW_{433K}/C; <1 mV for NW_{493K}/C; 11 mV for NW_{553K}/C.

ICP-MS measurements after the ADT determined the Pt:Ni atomic ratio of each PtNi NW as follows: NW_{433K}/C_af is $Pt_{99}Ni_1$, NW_{493K}/C_af is $Pt_{88}Ni_{12}$ and NW_{553K}/C_af is $Pt_{90}Ni_{10}$ (**Table S2**). The most durable NW_{493K}/C_af has the highest Ni atomic ratio. In contrast, NW_{433K}/C_af has lost almost all of the Ni contents. Pt dissolution is also suppressed for NW_{443K}/C: NW_{443K}/C_af loss 6.1% of Pt in weight, NW_{443K}/C_af loss 4.3% and 9.7% for NW_{553K}/C_af. Thus, NW_{493K}/C_af is most durable and maintains high Ni contents.

Practical H_2-air fuel cell measurements of NW_{493K}/C were also performed (**Figure 4**). The current densities at 0.5 V slightly increased from 761 to 832 mA cm^{-2} after 2000 square-wave potential cycles at 353 K, indicating that NW_{493K}/C tend to be more durable than other NWs.[32] The open circuit voltage (OCV) increased from 0.945 V vs. RHE to 0.958 V vs. RHE after the potential cycles, keeping ECSAs of about 55 m^2 g^{-1} based on the amount of Pt. The power density reaches

about 490 mW cm^{-2}, which is higher than the maximum power density previously reported for Pt NWs used at the cathode in an MEA.[9]

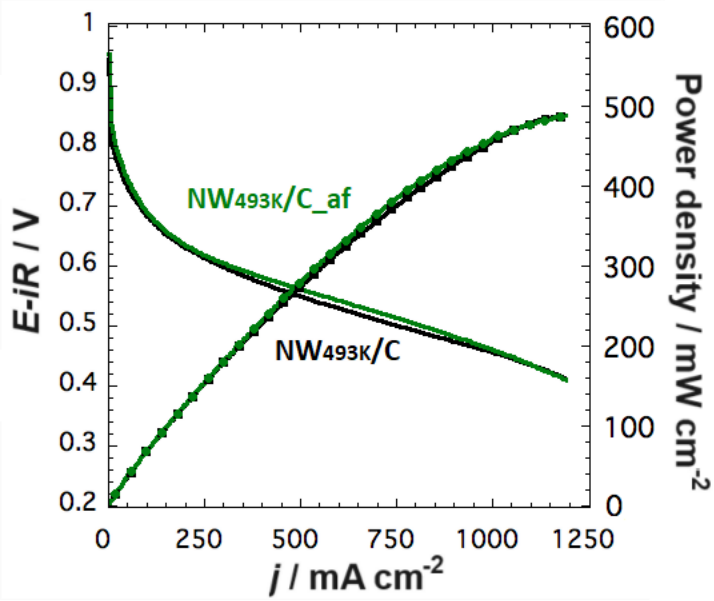

Figure 4. Current-voltage (*I-V*) curves and power density curves for the of NW_{493K}/C and NW_{493K}/C_af.

To investigate the origin of ORR electrocatalytic durability and suppression of Pt and Ni dissolution, STEM was taken after ADTs (**Figure 5a–c**). A unique morphological transformation occurred on NW_{493K}/C_af: PtNi NWs were transformed into beads-on-nanowires (**Figure 5b**). NW_{433K}/C was also changed similarly to waved and branched structures, as previously reported.[3] In contrast, NW_{553K}/C was converted into a branched structure with no waved structure or beads. Because the NW_{493K}/C catalyst has both sufficient Ni contents and co-existing PtNi NPs, the structural change could be mediated by the dissolution-redeposition process under potential cycles involving the co-existing PtNi NPs. High Ni contents can ensure that PtNi is well alloyed even after potential cycles to keep the catalytic activity. The STEM-EDS mapping images and STEM-EDS line profile analysis data of NW_{493K}/C_af indicate that the beads-on-nanowires have a Pt-rich bone wrapped with PtNi-core and Pt-skin (**Figure 5d–g** and **Figure S5**) Beads-on-nanowires of

NW_{493K}/C_af have the Pt-rich bone with a diameter of about 2 nm (**Figure 5b**) and the Pt-rich skin with 2–6 Pt-rich layers (**Figure 5h** and **Figure S5b**). No such Pt-rich bone or skin was confirmed in STEM-EDS mapping images and line profile analysis of NW_{433K}/C_af and NW_{553K}/C_af (**Figure S6)**.

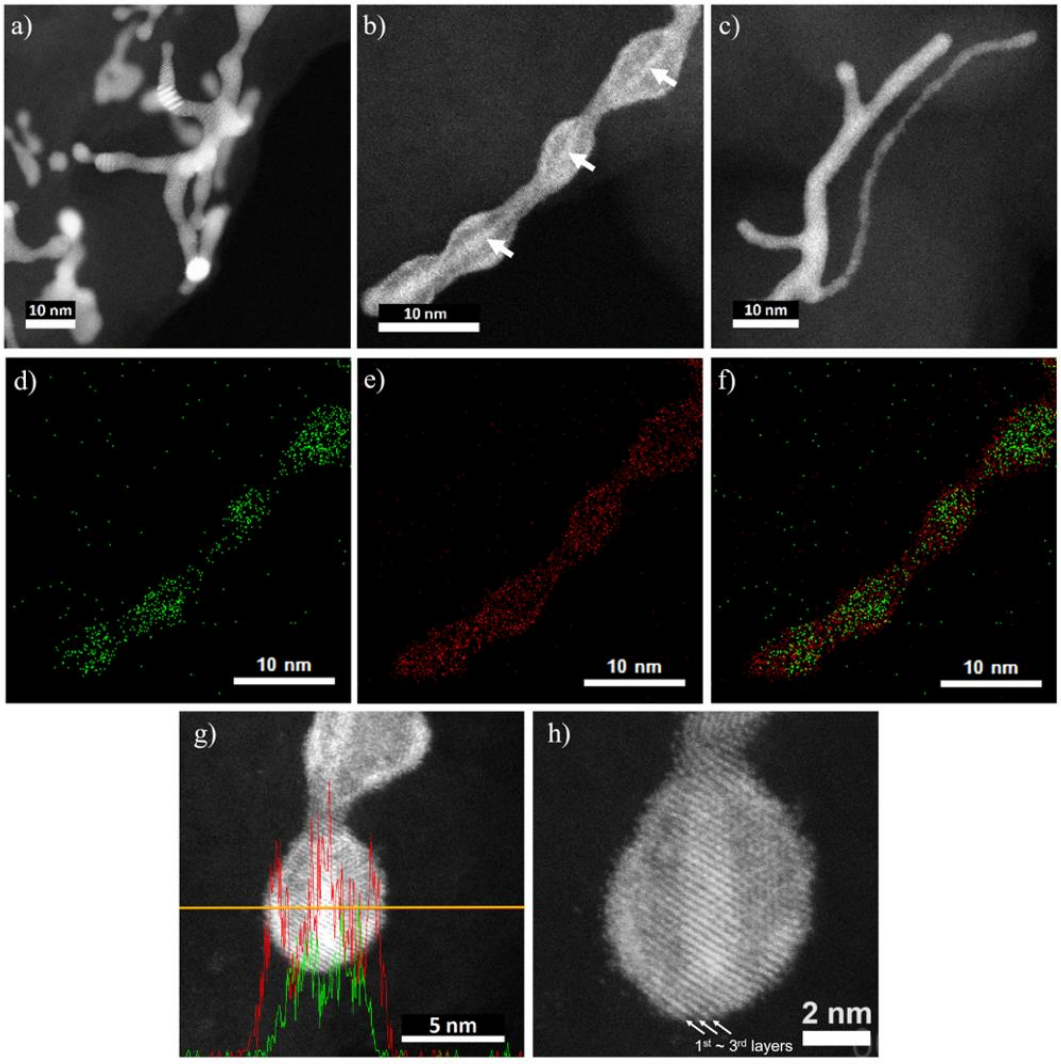

Figure 5. HAADF-STEM images of (a) NW_{433K}/C_af, (b) NW_{493K}/C_af and (c) NW_{553K}/C_af. The arrows in (b) highlight the formation of a bone in the beads-on-nanowire. The STEM-EDS mapping images of (d) Ni-*K*, (e) Pt-*M* and (f) Pt-Ni overlay. (g) An EDS line profile of NW_{493K}/C_af. The lines in red, green and orange indicate the Ni-*K* signal, Pt-*M* signal, and the

position of the line profile analysis, respectively. Another line profile of NW_{493K}/C_af at a different position is available in **Figure S5**. EDS line profiles of NW_{433K}/C_af and NW_{553K}/C_af are found in **Figure S6**. (h) A STEM image of NW_{493K}/C_af. The arrows in white indicate plausible Pt-rich layers for the Pt-skin.

Comparison between CO stripping voltammograms before and after the ADT shows changes in surface structures and electronic states. For NW_{433K}/C, the CO oxidative desorption peak potential shifted from 0.84 V vs. RHE to 0.83 V vs. RHE, and a shoulder peak appeared at 0.76 V vs. RHE after ADT (**Figure 6**). For NW_{493K}/C, the peak at 0.85 V vs. RHE was shifted to 0.83 V vs. RHE after ADT. For NW_{553K}/C, the peak shape and peak potential did not change before and after ADT but charges involving CO oxidation decreased. Because CO oxidative desorption potentials are sensitive to surface structures,[3,9,33–36] electronic changes of the surface Pt occurred for NW_{433K}/C_af and NW_{493K}/C_af but not for NW_{553K}/C. [37,38] Note that compared to NW_{433K}/C_af, the shoulder peak growth of NW_{493K}/C_af is more obvious. The shoulder peak of CO oxidation desorption originates from CO oxidation on lower coordinated Pt sites.[36,39] Since Ostwald ripening assisted by the co-existing PtNi NPs occurred on NW_{433K}/C_af and NW_{493K}/C_af (**Figure 5**), it initiates morphological and surface changes, producing such lower coordinated Pt sites for NW_{493K}/C_af. Furthermore, the ratio of ECSA calculated from the Faradaic charge of CO oxidative desorption ($ECSA_{CO}$) to $ECSA_H$ is 1.49 for NW_{493K}/C_af (**Table 1**), which also indicates that the Pt skin was formed on beads-on-nanowires.[40,41] As the result, NW_{493K}/C_af keeps the ECSA and activity even after the ADT.

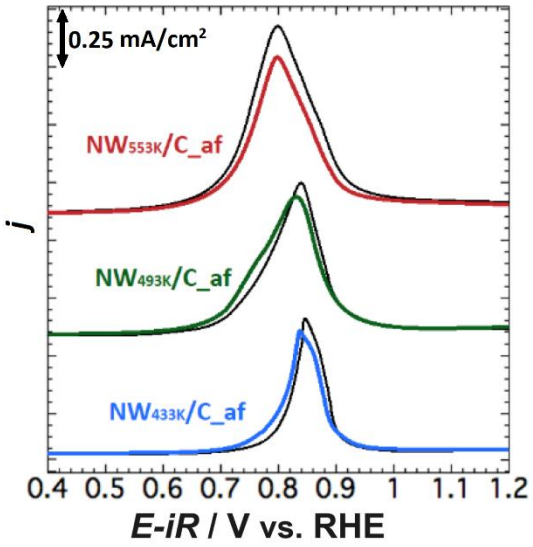

Figure 6. CO stripping voltammograms of NW_{433K}/C_af (in blue), NW_{493K}/C_af (in green) and NW_{553K}/C_af (in red) recorded at 50 mV s^{-1} in a 0.1 M $HClO_4$ aqueous solution under Ar. The black traces are CO stripping voltammograms of the corresponding catalysts before the ADT.

We also compared CVs of each electrocatalyst recorded under Ar before and after ADT to support surface changes after the ADT (**Figure S4**). An anodic wave ≥0.8 V vs. RHE, which is associated with Pt-O(H) formation, decreased after ADT. Thus, the structural change tends to suppress the Pt-O(H) formation. It is also known that anodic waves ranging between 0.05 and 0.4 V vs. RHE involve the hydrogen desorption from the Pt surface and their potential is sensitive to the surface atom arrangement of Pt. [42] An anodic peak at about 0.1 V vs. RHE tend to be higher than that at 0.3 V after ADT particularly for NW_{493K}/C. The structural transformation of NW_{493K}/C to the beads-on-nanowire could produce Pt(111)-rich domains at the Pt surface.

To further clarify the electrocatalytic performance changes brought by the structural transformation into Pt-skin beads-on-nanowires, *in situ* XAS measurements of NW_{493K}/C and NW_{493K}/C_af were performed in the Pt L_3-edge region (**Figure 7**). The white line intensity in the

X-ray absorption near edge structure (XANES) region is known to be associated with the 2p → 5d transition and reflect the degree of vacancy of the Pt 5d orbitals near the Fermi level, and therefore the intensities are sensitive to changes in the oxidation state of Pt.[43] *In situ* XAS measurements of NW_{493K}/C and NW_{493K}/C_af in a 0.1 M $HClO_4$ aqueous solution under Ar reveal that NW_{493K}/C shows much larger changes in white line intensity than NW_{493K}/C_af (**Figure 7c**). This result indicates that the oxidation of Pt species at the surface is clearly suppressed on the Pt skin of NW_{493K}/C_af because of the down-shift of the surface Pt *d*-band center position, [3,6,34,44,45] which is in good agreement with the results of CVs recorded under Ar (**Figure S4b**). The suppression of the Pt oxidation is effective to improve the durability because of the inhibition of the chemical dissolution *via* Pt-O species ($Pt\text{-}O + 2H^+ \rightarrow Pt^{2+} + H_2O$).[46] Similar effects on the durability are also reported for Pt-alloy nanostructured electrocatalysts with the Pt-skin.[17–19]

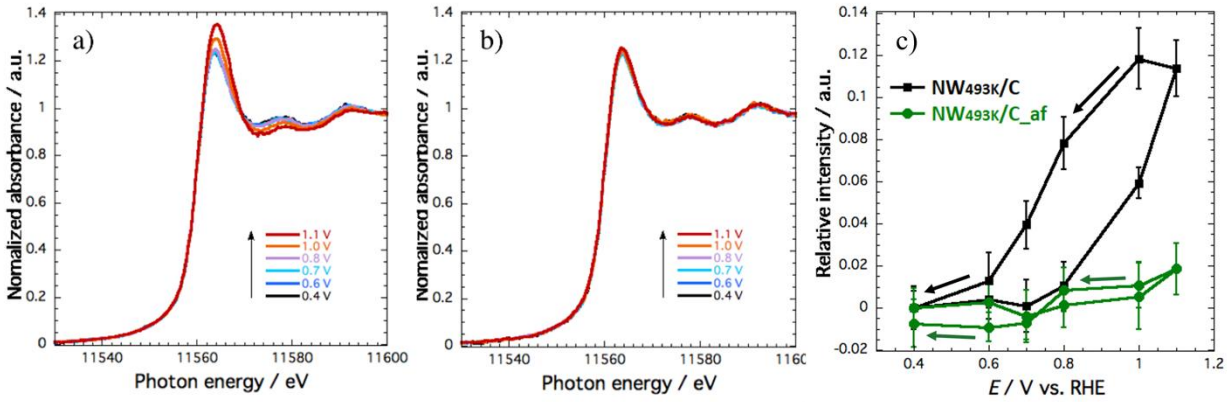

Figure 7. *In situ* XANES spectra of (a) NW_{493K}/C and (b) NW_{493K}/C_af. (c) Plots of relative white line peak intensities of NW_{493K}/C and NW_{493K}/C_af against potential. Potentials were applied stepwise from +0.4 to +1.1 V vs. RHE in a 0.1 M $HClO_4$ aqueous solution under nitrogen. Averaged data points of white line intensities ranging from 11563 to 11565 eV in photon energy were plotted in relative to the initial intensity at +0.4 V vs RHE. XANES spectra

of potentials step back from +1.1 to +0.4 V vs RHE and enlarged spectra in the white line region are available in **Figure S7**.

Based on our experimental results, we propose the structural transformation of PtNi NWs and NPs to beads-on-nanowires for NW_{493K}/C after the ADT (**Figure 8)**. Because NWs are more difficult to dissolve and degrade than NPs in potential cycling,[7,9,10,14,15] PtNi NPs can be dissolved and then reduced to the nanowires via Ostwald ripening.[3] The newly produced surface has a large number of surface defects, [20,30] which enable the nucleation of the PtNi alloy phase on the surface and then form PtNi alloy beads-on-nanowires. [20] After the co-present NPs deplete, the near-surface Ni contents in the PtNi alloy beads begin to be etched during potential cycling, resulting in the formation of the Pt skin,[22] which is proved by HAADF-STEM and EDS mapping images (**Figure 5**) and CO stripping voltammograms (**Figure 6**). Unlike other PtM nanostructured catalysts with the Pt skin, the Pt-skin of the beads-on-nanowires that we report arises spontaneously *via* Ostwald ripening assisted by the co-existing PtNi NPs during potential cycling, rather than commonly used acid etching [17,18,22] or reductive deposition of an additional Pt complex during preparation. [19,20,23] The formation of PtNi alloy beads-on-nanowires of NW_{493K}/C_af with 11.8 at% of Ni (**Table S2**) and the Pt skin suppresses the Pt-O(H) formation *via* ligand effects,[18,47] leading to the improvement of the durability.

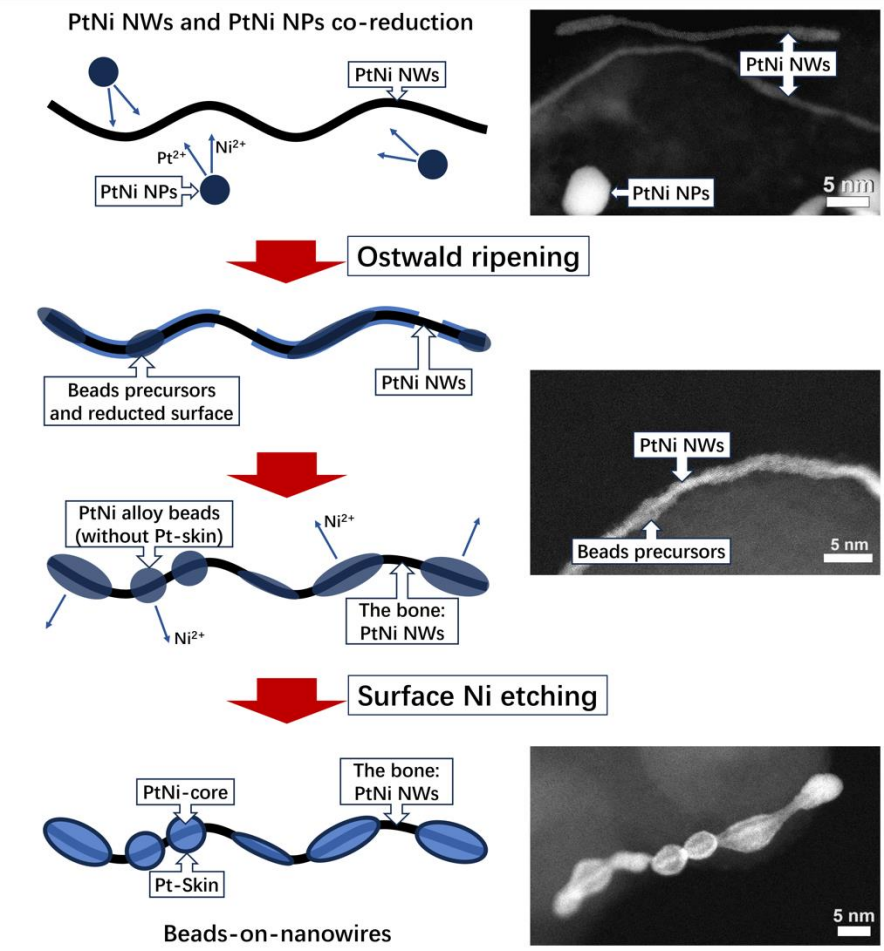

Figure 8. Proposed mechanism of the PtNi beads-on-nanowires for NW_{493K}/C during the ADT (left) and corresponding STEM images (right) via Ostwald ripening of co-existing PtNi NPs to PtNi NWs.

CONCLUSIONS

We prepared the PtNi NWs at 433, 493 and 533 K as ORR electrocatalysts. The higher temperature gives more Ni contents in PtNi NWs and NW_{433K} and NW_{493K} have co-existing PtNi NPs. After the ADT, PtNi NW_{493K} is transformed into beads-on-nanowires with the Pt-skin and bone. The sufficient Ni contents and Ostwald ripening by co-presence of PtNi NPs result in its structural transformation. The transformed beads-on-nanowires are durable against both Pt and Ni

dissolution. The surface electronic structure was also changed for PtNi NW_{493K}/C after the ADT. Oxygenated species at the Pt surface are suppressed, leading to the high durability.

This work demonstrates that the synthesis temperature for PtNi NWs is sensitive to Ni contents and the presence or absence of PtNi NPs. The higher synthesis temperature does not always give durable PtNi NWs. The Ostwald-ripening of the co-existing PtNi NPs under potential cycles assists the structural transformation into highly durable beads-on-nanowires. Our work suggests that the synthesis and design of self-optimized nanostructured catalysts initiated by external stimuli such as potential cycles would be important to develop highly durable electrocatalysts.

EXPERIMENTAL SECTION

Materials.

Oleylamine, $[Pt(acac)_2]$ (acac = acetylacetonato), D(+)-glucose, cyclohexane, 2-propanol, 5% Nafion DE520 and perchloric acid were purchased from Wako Pure Chemical Industries, Ltd. $[Ni(acac)_2]$, $[Mo(CO)_6]$ and Pt/C (TEC10V30E) were commercially available from Sigma-Aldrich, Kanto Chemical and Tanaka Kikinzoku Kogyo, respectively. Ethanol and Hexadecyltrimethylammonium chloride (CTAC) were purchased from Hokkai-Chemy and Tokyo Chemical Industry Co. Ltd, respectively. Pure argon gas (99.9995%, Hokkaido Air Water), pure oxygen gas (99.995%, Air Liquide Japan) and CO gas (99.9%, GL Science) were used for electrochemical measurements.

Synthesis of PtNi NWs with or without PtNi NPs.

PtNi NWs were synthesized using a modified procedure that was previously reported.[3] 5 mL of oleylamine (15 mmol),10 mg of $[Pt(acac)_2]$ (0.025 mmol), 6.4 mg of $[Ni(acac)_2]$ (0.025 mmol), 10 mg of CTAC (0.031 mmol), 20 mg of $[Mo(CO)_6]$ (0.075 mmol) and 60 mg of D-glucose (0.33

mmol) was added into a 100 mL double-necked round bottom flask. The mixture was dispersed by ultrasonication for 30 minutes in a water-bath at 298 K and then stirred at 343 K under Ar for 10 min. When the solution mixture becomes transparent and yellowish-green, it was transferred to a pre-heated oil bath at 433, 493 or 533 K under Ar for 2 h and keep stirring. After heating, a solution mixture of ethanol and cyclohexane (ca.15 mL, 4:1, *v*/*v*) was added to the reaction mixture to rinse once it had naturally cooled to room temperature in the air. Then the mixture was repeatedly centrifuged at 9500 rpm and 298 K and rinsed for at least seven times to obtain PtNi NWs with or without PtNi NPs, depending on the heating temperature. The products prepared at 433, 493 and 553 K are denoted as NW_{433K}, NW_{493K} and NW_{553K}, respectively. The products were stored in ethanol at room temperature until use. Yields of PtNi NWs are ca. 6 mg.

Vulcan XC-72R (ca. 3 mg) and PtNi NWs (ca. 1 mg) were dispersed in 15 mL of a mixture of ethanol and cyclohexane (1:1, *v*/*v*), placed in an ice-water mixture, and then ultrasonicated for at least 5 hours. The carbon-supported PtNi NWs were repeatedly centrifuged at 9500 rpm and 298 K for at least five times. After each centrifugation, the compound was washed with around 15 mL of a mixture of ethanol and cyclohexane solvent (4:1, *v*/*v*). The composite was stored in a minimal amount in ethanol (ca. 2 mL) at room temperature.

Physicochemical measurements.

STEM images were obtained at 200 kV acceleration voltage using an HD-2000 (Hitachi Scientific Instrument). A JEOL JEM-ARM200F instrument was then used to obtain HAADF-STEM images and STEM-EDS elemental mapping at 200 kV.

XRD was taken at a voltage of 30 kV and a current of 10 mA using Ni-filtered Cu Kα radiation (λ = 1.5406 Å) on an X-ray diffractometer D2 PHASER (Burker). For sample preparation, a

catalyst powder which was loaded on the Vulcan XC-72R before potential cycles, was paved on the acrylic cell.

ICP–MS was conducted with an ICP–MS spectrometer 8800 ICP-QQQ (Agilent Technologies). For the preparation of the sample, the catalyst was scraped off from the GC electrode after use, and then dispersed in aqua regia solution and stirred at a temperature of 308 K for at least 24 hours. The dispersion was filtered through a membrane filter (13HP045AN, ADVANTEC), and then the filtrate was diluted with Milli-Q water.

Electrochemical measurements.

All electrochemical measurements were performed using a conventional three-electrode setup. A potentiostat (HZ-7000, Hokuto Denko) was used to record CVs and LSVs. An Ag|AgCl (sat. KCl) electrode (International chemistry Co., Ltd) with a double junction holder and platinum foil were used as the reference electrode and the counter electrode, respectively. A rotating disk electrode (RDE) with a catalyst-modified GC was used as the working electrode.

A GC (screw type or disk type,5 mm φ, M4, Tokai Carbon Co., Ltd.) was polished using alumina slurry (0.3 μm, Baikalox), followed by alumina slurry (0.05 μm, Baikalox). Subsequently, it was ultrasonicated in acetone and Milli-Q water for at least 5 min each before a catalyst ink was drop-cast. The catalyst ink was prepared in the following proportions: 14 mg of the catalyst, 6 mL of 2-propanol, 19 mL of Milli-Q water, and 100 μL of 5% Nafion DE520. The mixture was dispersed under ultrasonication for at least 2 hours in an ice water mixture bath. Drop the catalyst ink (ca. 10 μL) onto the GC disc and leave for ca. 1 hour at room temperature, rotating at 400 rpm using an AFMSRX Analytical Rotator and MSRX Speed Controller (PINE Research Instrumentation) until the ink has dried. CVs and LSVs were recorded in a 0.1M $HClO_4$ aqueous solution as the electrolyte solution. The electrolyte solution must be purged with argon or oxygen for a minimum

of 30 minutes prior to the electrochemical measurements. Before collecting the CVs and LSVs shown in this work, electrochemical cleaning was performed by 50 potential cycles at 100 mV s^{-1} in the potential range between 0.1 and 1.0 V vs. RHE in the Ar-purged 0.1 M $HClO_4$ aqueous solution. All LSVs under oxygen are corrected by the subtraction of the current densities of the corresponding working electrode recorded under Ar. All potentials in CVs and LSVs are shown against the RHE after *iR* correction. A solution resistance was determined to be 34 Ω by electrochemical impedance spectroscopy using a potentiostat of HZ7000 and then used for the *iR* correction.

For the ADT, to increase the adhesion between the GC and the catalyst film, the catalyst modified GC screws were heated at 418 K for 10 minutes. The ADT was performed at 353 K in 0.1 M $HClO_4$ solution under Ar with 2000 square-wave potential steps between +0.6 and +0.9 V vs. RHE holding for 3 s at each potential. A porous carbon electrode (BAS) was used as the counter electrode.

For CO stripping measurements, a 0.1 M $HClO_4$ aqueous electrolyte solution was purged with CO for 10 min and then with Ar for 60 min. During purging, a fixed potential of 0.05 V vs. RHE was applied to the working electrode until measurements were started. Two cycles of CVs, the first cycle for CO stripping voltammetry and the second cycle for the background, were recorded in the potential range from 0.05 to 1.45 V vs. RHE at 50 mV s^{-1} in an Ar-purged 0.1 M $HClO_4$ aqueous solution. Based on the difference between the first and second cycles, the electrochemical oxidation of CO observed in the first cycle ($ECSA_{CO}$) and the desorption of hydrogen observed in the second cycle ($ECSA_H$) were determined.

We determined the mass activity (MA) using the kinetically controlled current density (j_k) at +0.9 V vs. RHE and the amount of Pt on the GC electrode. J_k was obtained based on the Koutechy-

Levich plot from LSVs taken at different rotational speeds of 100 rpm, 400 rpm, 900 rpm, 1600 rpm and 2500 rpm (**Figure S8**). The amount of Pt was determined by ICP-MS. The specific activity (SA) was calculated based on the j_k and $ECSA_H$.

H_2-air fuel cell measurements

Practical H_2-air fuel cell measurements were performed for NW_{493K}/C as the cathode catalyst. A membrane electrode assembly (MEA) is made in the following method: For the cathode side, 71.9 mg of NW_{493K}/C was dispersed under ultrasonication in 366 μL of Milli-Q water, 3,293 μL of ethanol, and 510 μL of 5% Nafion DE520 to make the catalyst ink. The catalyst ink was spray-printed using a spraying device (C-3 J, Nordson K.K.) on one side of a Nafion 212 membrane (4 × 6 cm^2) within an of 1 × 1 cm^2 area to obtain NW_{493K} with a metal loading density of 0.3 mg cm^{-2}. In the same way, the anode ink of Pt/C (TEC10E50E) was prepared on the other side of Nafion 212 membrane to achieve the Pt amount of 0.3 mg cm^{-2}. Ionomer Nafion contents used in the cathode and anode catalyst layers were 24 and 28 wt%, respectively. The catalyst-coated Nafion films were hot-pressed at 16 N cm^{-2} using a digital press (CYPT-10, SINTOKOGIO, LTD.) at 132 °C for 190 s. The hot-pressed catalyst-coated film was sandwitched with two pieces of carbon papers (EC-TP1-060T, TORAY Industry, Inc.) to complete the MEA. Finally, the MEA was placed in a cell holder designed in the previous NEDO project and made at Japan FC Planning. Serpentine flow-field design was applied.

Current-voltage (*I-V*) characteristics were evaluated at 80°C-RH100%. The 139 cc/min of RH 100% H_2 and 332 cc/min of RH100% air were flowed into the anode and the cathode, respectively. Before actual *I–V* measurements, as a pretreatment step, the constant voltage of 0.6 V was applied for 4 hours while supplying humidified gases. The conditions for the ADT experiments of the MEAs were the same as those of the RDE: 2000 potential cycles by using a square wave between

the potentials at +0.6 V for 3 s and +0.9 V for 3 s at 353 K. The *I–V* curves were also recorded after ADT. The measurements were performed with a constant potential meter (SP-300, BioLogic Inc.). *I–V* measurements were carried out using a PEM power generation measurement device AutoPEM-KUG2 (Toyo Co.) and a potentiostat SP-240 (BioLogic Inc.).

XAS measurements.

In situ XAS data of PtNi NW_{493K}/C after the ADT were collected in the fluorescent method using a 19-element Ge solid state detector at BL14B2 station in SPring-8. A home-build spectroelectrochemical flow cell **(Figure S9)** with three electrodes was used.[48] A carbon foil (Permafoil, 0.1 mm in thickness, Toyo Tanso) was used as the working electrode with PtNi NWs/C catalysts drop-casted on it, and the ADT, 2000 potential cycles were performed using a square wave between the potentials at +0.6 V vs. RHE for 3 s and +0.9 V vs. RHE for 3s at 353 K in 0.1 M $HClO_4$ solution under Ar. A GC rod (R-3, 3 mm φ, BAS) and an Ag|AgCl electrode (Innovative Instruments, Inc.) with a double junction holder was used as the counter and reference electrodes, respectively. Before *in situ* XAS measurements, a 0.1 M $HClO_4$ aqueous electrolyte solution was purged with N_2 for at least 30 min, followed by 50 potential cycles at 100 mV s^{-1} in the potential range of 0.1 V vs. RHE to 1.0 V vs. RHE under N_2 for electrochemical cleaning. XAS spectra of the catalysts were obtained at 0.4, 0.6, 0.7, 0.8, 1.0 and 1.1 V vs. RHE. XANES spectra were normalized using Athena software (Demeter 0.9.26).[49]

AUTHOR INFORMATION

Corresponding Authors

Emails: masaru.kato@ees.hokudai.ac.jp (MK); iyagi@ees.hokudai.ac.jp (IY)

ASSOCIATED CONTENT

Supporting Information.

The Supporting Information are available free of charge.

Length distributions of NWs, X-ray diffraction patterns, CVs under Ar, *I-V* curve of H_2-air fuel cell, beads-on-nanowire evolution illustration, high-resolution STEM images, STEM-EDS mapping images, line profile analysis images, EXAFS oscillations and Fourier-transforms of the EXAFS oscillations, potential dependent and enlarged XANES spectra, images of our spectro-electrochemical flow cell, Pt contents before and after potential cycles, and parameters used for EXAFS curve-fitting analysis. (PDF)

ACKNOWLEDGMENTS

The authors thank Shingo Mukai, Yusuke Kawamura (Technical Division, Institute for Catalysis, Hokkaido University), and Takao Ohta (Graduate School of Engineering, Hokkaido University) for their technical support on electrochemical setups; Naomi Hirai and Yuko Mori (Research Institute for Electronic Science, Hokkaido University) for taking the STEM, HAADF−STEM and EDS mapping images, Prof. Noro Shinichiro (Graduate School of Environmental Science, Hokkaido University) for taking XRD patterns. This work was supported by the Nanotechnology

Platform program of the Ministry of Education, Culture, Sports, Science and Technology (MEXT) for Hokkaido University (JPMXP09A17HK0073, JPMXP09A18HK0063, JPMXP09A19HK0030 and JPMXP09A21HK0062) and Institute for Molecular Science (JPMXP09S18MS0029), "Advanced Research Infrastructure for Materials and Nanotechnology in Japan (ARIM)" of the MEXT (JPMXP1222HK0033 and JPMXP1223HK0012) and the New Energy and Industrial Technology Development Organization (NEDO) (JPNP20003). XAS measurements were performed at BL14B2, SPring-8, Japan (2022B0608 and 2023A1791).

REFERENCES

(1) Kwon, T.; Jun, M.; Lee, K. Catalytic Nanoframes and Beyond. *Adv. Mater.* **2020**, *32*, 2001345.

(2) Jiang, K.; Zhao, D.; Guo, S.; Zhang, X.; Zhu, X.; Guo, J.; Lu, G.; Huang, X. Efficient Oxygen Reduction Catalysis by Subnanometer Pt Alloy Nanowires. *Sci. Adv.* **2017**, *3*, 2–10.

(3) Kato, M.; Iguchi, Y.; Li, T.; Kato, Y.; Zhuang, Y.; Higashi, K.; Uruga, T.; Saida, T.; Miyabayashi, K.; Yagi, I. Structural Transformation of Pt–Ni Nanowires as Oxygen Reduction Electrocatalysts to Branched Nanostructures during Potential Cycles. *ACS Catal.* **2022**, *12*, 259–264.

(4) Wang, K.; Wang, Y.; Geng, S.; Wang, Y.; Song, S. High-Temperature Confinement Synthesis of Supported Pt–Ni Nanoparticles for Efficiently Catalyzing Oxygen Reduction Reaction. *Adv. Funct. Mater.* **2022**, *32*, 2113399.

(5) Greeley, J.; Stephens, I. E. L.; Bondarenko, A. S.; Johansson, T. P.; Hansen, H. A.; Jaramillo, T. F.; Rossmeisl, J.; Chorkendorff, I.; Nørskov, J. K. Alloys of Platinum and Early Transition Metals as Oxygen Reduction Electrocatalysts. *Nat. Chem.* **2009**, *1*, 552–556.

(6) Kato, M.; Ogura, K.; Nakagawa, S.; Tokuda, S.; Takahashi, K.; Nakamura, T.; Yagi, I. Enhancement of Electrocatalytic Oxygen Reduction Activity and Durability of Pt-Ni Rhombic Dodecahedral Nanoframes by Anchoring to Nitrogen-Doped Carbon Support. *ACS Omega* **2018**, *3*, 9052–9059.

(7) Li, M.; Zhao, Z.; Cheng, T.; Fortunelli, A.; Chen, C. Y.; Yu, R.; Zhang, Q.; Gu, L.; Merinov, B. v.; Lin, Z.; Zhu, E.; Yu, T.; Jia, Q.; Guo, J.; Zhang, L.; Goddard, W. A.; Huang, Y.; Duan, X. Ultrafine Jagged Platinum Nanowires Enable Ultrahigh Mass Activity for the Oxygen Reduction Reaction. *Science* **2016**, *354*, 1414–1419.

(8) Sun, Y.; Luo, M.; Qin, Y.; Zhu, S.; Li, Y.; Xu, N.; Meng, X.; Ren, Q.; Wang, L.; Guo, S. Atomic-Thick PtNi Nanowires Assembled on Graphene for High-Sensitivity Extracellular Hydrogen Peroxide Sensors. *ACS Appl. Mater. Interf.* **2017**, *9*, 34715–34721.

(9) Kong, F.; Norouzi Banis, M.; Du, L.; Zhang, L.; Zhang, L.; Li, J.; Doyle-Davis, K.; Liang, J.; Liu, Q.; Yang, X.; Li, R.; Du, C.; Yin, G.; Sun, X. Highly Stable One-Dimensional Pt Nanowires with Modulated Structural Disorder towards the Oxygen Reduction Reaction. *J. Mater. Chem. A* **2019**, 24830–24836.

(10) Bu, L.; Guo, S.; Zhang, X.; Shen, X.; Su, D.; Lu, G.; Zhu, X.; Yao, J.; Guo, J.; Huang, X. Surface Engineering of Hierarchical Platinum-Cobalt Nanowires for Efficient Electrocatalysis. *Nat. Commun.* **2016**, *7*, 11850.

(11) Gong, M.; Deng, Z.; Xiao, D.; Han, L.; Zhao, T.; Lu, Y.; Shen, T.; Liu, X.; Lin, R.; Huang, T.; Zhou, G.; Xin, H.; Wang, D. One-Nanometer-Thick Pt3Ni Bimetallic Alloy Nanowires Advanced Oxygen Reduction Reaction: Integrating Multiple Advantages into One Catalyst. *ACS Catal.* **2019**, *9*, 4488–4494.

(12) Yoon, J.; Park, J.; Sa, Y. J.; Yang, Y.; Baik, H.; Joo, S. H.; Lee, K. Synthesis of Bare Pt3Ni Nanorods from PtNi@Ni Core-Shell Nanorods by Acid Etching: One-Step Surfactant Removal and Phase Conversion for Optimal Electrochemical Performance toward Oxygen Reduction Reaction. *CrystEngComm* **2016**, *18*, 6002–6007.

(13) Wang, X.; Li, Z.; Qu, Y.; Yuan, T.; Wang, W.; Wu, Y.; Li, Y. Review of Metal Catalysts for Oxygen Reduction Reaction: From Nanoscale Engineering to Atomic Design. *Chem*. **2019**, *13*, 1486–1511.

(14) Lin, R.; Cai, X.; Zeng, H.; Yu, Z. Stability of High-Performance Pt-Based Catalysts for Oxygen Reduction Reactions. *Adv. Mater.* **2018**, *30*, 1705332.

(15) Zhao, Z.; Chen, C.; Liu, Z.; Huang, J.; Wu, M.; Liu, H.; Li, Y.; Huang, Y. Pt-Based Nanocrystal for Electrocatalytic Oxygen Reduction. *Adv. Mater.* **2019**, *31*, 1808115.

(16) Kodama, K.; Nagai, T.; Kuwaki, A.; Jinnouchi, R.; Morimoto, Y. Challenges in Applying Highly Active Pt-Based Nanostructured Catalysts for Oxygen Reduction Reactions to Fuel Cell Vehicles. *Nat. Nanotechnol.* **2021**, *16*, 140–147.

(17) Li, J.; Xi, Z.; Pan, Y. T.; Spendelow, J. S.; Duchesne, P. N.; Su, D.; Li, Q.; Yu, C.; Yin, Z.; Shen, B.; Kim, Y. S.; Zhang, P.; Sun, S. Fe Stabilization by Intermetallic L10-FePt and Pt Catalysis Enhancement in L10-FePt/Pt Nanoparticles for Efficient Oxygen Reduction Reaction in Fuel Cells. *J. Am. Chem. Soc.* **2018**, *140*, 2926–2932.

(18) Chen, C.; Kang, Y.; Huo, Z.; Zhu, Z.; Huang, W.; Xin, H. L.; Snyder, J. D.; Li, D.; Herron, J. A.; Mavrikakis, M.; Chi, M.; More, K. L.; Li, Y.; Markovic, N. M.; Somorjai, G. A.; Yang, P.; Stamenkovic, V. R. Highly Crystalline Multimetallic Nanoframes with Three-Dimensional Electrocatalytic Surfaces. *Science* **2014**, *343*, 1339–1343.

(19) Tian, X.; Zhao, X.; Su, Y.-Q.; Wang, L.; Wang, H.; Dang, D.; Chi, B.; Liu, H.; Hensen, E. J. M.; Lou, X. W. (David); Xia, B. Y. Engineering Bunched Pt-Ni Alloy Nanocages for Efficient Oxygen Reduction in Practical Fuel Cells. *Science* **2019**, *366*, 850–856.

(20) Jin, H.; Xu, Z.; Hu, Z. Y.; Yin, Z.; Wang, Z.; Deng, Z.; Wei, P.; Feng, S.; Dong, S.; Liu, J.; Luo, S.; Qiu, Z.; Zhou, L.; Mai, L.; Su, B. L.; Zhao, D.; Liu, Y. Mesoporous Pt@Pt-Skin Pt_3Ni Core-Shell Framework Nanowire Electrocatalyst for Efficient Oxygen Reduction. *Nat. Commun.* **2023**, *14*, 1518.

(21) Liu, M.; Zhao, Z.; Duan, X.; Huang, Y. Nanoscale Structure Design for High-Performance Pt-Based ORR Catalysts. *Adv. Mater.*, **2019**, *31*, 1802234.

(22) Xie, M.; Lyu, Z.; Chen, R.; Shen, M.; Cao, Z.; Xia, Y. Pt-Co@Pt Octahedral Nanocrystals: Enhancing Their Activity and Durability toward Oxygen Reduction with an Intermetallic Core and an Ultrathin Shell. *J. Am. Chem. Soc.* **2021**, *143*, 8509–8518.

(23) Weber, P.; Weber, D. J.; Dosche, C.; Oezaslan, M. Highly Durable Pt-Based Core-Shell Catalysts with Metallic and Oxidized Co Species for Boosting the Oxygen Reduction Reaction. *ACS Catal.* **2022**, *12*, 6394–6408.

(24) Haile, A. S.; Yohannes, W.; Mekonnen, Y. S. Oxygen Reduction Reaction on Pt-Skin $Pt_3V(111)$ Fuel Cell Cathode: A Density Functional Theory Study. *RSC Adv* **2020**, *10*, 27346–27356.

(25) Zheng, Y.; Petersen, A. S.; Wan, H.; Hübner, R.; Zhang, J.; Wang, J.; Qi, H.; Ye, Y.; Liang, C.; Yang, J.; Cui, Z.; Meng, Y.; Zheng, Z.; Rossmeisl, J.; Liu, W. Scalable and Controllable Synthesis of Pt-Ni Bunched-Nanocages Aerogels as Efficient Electrocatalysts for Oxygen Reduction Reaction. *Adv. Energy Mater.* **2023**, *13*, 2204257.

(26) Lv, P.; Jin, B.; Mei, C.; Zhou, H.; Yuan, T.; Li, Z.; He, H.; Shen, X.; Hong, X. Pt9Ni Wavelike Nanowires with High Activity for Oxygen Reduction Reactions. *Chem. - A Eur. J.* **2018**, *24*, 14636–14638.

(27) Chattot, R.; Martens, I.; Scohy, M.; Herranz, J.; Drnec, J.; Maillard, F.; Dubau, L. Disclosing Pt-Bimetallic Alloy Nanoparticle Surface Lattice Distortion with Electrochemical Probes. *ACS Energy Lett.* **2020**, *5*, 162–169.

(28) Wang, C.; Hou, Y.; Kim, J.; Sun, S. A General Strategy for Synthesizing FePt Nanowires and Nanorods. *Angew. Chem. Int. Ed.* **2007**, *46*, 6333–6335.

(29) Xu, H.; Wei, J.; Zhang, M.; Wang, C.; Shiraishi, Y.; Guo, J.; Du, Y. Solvent-Mediated Length Tuning of Ultrathin Platinum-Cobalt Nanowires for Efficient Electrocatalysis. *J. Mater. Chem. A* **2018**, *6*, 24418–24424.

(30) Bu, L.; Ding, J.; Guo, S.; Zhang, X.; Su, D.; Zhu, X.; Yao, J.; Guo, J.; Lu, G.; Huang, X. A General Method for Multimetallic Platinum Alloy Nanowires as Highly Active and Stable Oxygen Reduction Catalysts. *Adv. Mater.* **2015**, *27*, 7204–7212.

(31) Petkov, V.; Maswadeh, Y.; Vargas, J. A.; Shan, S.; Kareem, H.; Wu, Z. P.; Luo, J.; Zhong, C. J.; Shastri, S.; Kenesei, P. Deviations from Vegard's Law and Evolution of the Electrocatalytic Activity and Stability of Pt-Based Nanoalloys inside Fuel Cells by: In Operando X-Ray Spectroscopy and Total Scattering. *Nanoscale* **2019**, *11*, 5512–5525.

(32) Cao J.; Cao H.; Wang f.; Zhu h. Zigzag PtCo nanowires modified in situ with Au atoms as efficient and durable electrocatalyst for oxygen reduction reaction. *J. Power Sources* **2021**, *489*, 229425

(33) Jiang, T.; Mowbray, D. J.; Dobrin, S.; Falsig, H.; Hvolbœk, B.; Bligaard, T.; Nørskov, J. K. Trends in CO Oxidation Rates for Metal Nanoparticles and Close-Packed, Stepped, and Kinked Surfaces. *J. Phys. Chem. C* **2009**, *113*, 10548–10553.

(34) Kato, M.; Nakahoshiba, R.; Ogura, K.; Tokuda, S.; Yasuda, S.; Higashi, K.; Uruga, T.; Uemura, Y.; Yagi, I. Electronic Effects of Nitrogen Atoms of Supports on Pt-Ni Rhombic Dodecahedral Nanoframes for Oxygen Reduction. *ACS Appl. Energy Mater.* **2020**, *3*, 6768–6774.

(35) Hodnik, N.; Dehm, G.; Mayrhofer, K. J. J. Importance and Challenges of Electrochemical in Situ Liquid Cell Electron Microscopy for Energy Conversion Research. *Acc. Chem. Res.* **2016**, *49*, 2015–2022.

(36) Urchaga, P.; Baranton, S.; Coutanceau, C.; Jerkiewicz, G. Electro-Oxidation of CO Chem on Pt Nanosurfaces: Solution of the Peak Multiplicity Puzzle. *Langmuir* **2012**, *28*, 3658–3663.

(37) Li, H.; Zhou, X.; Zhai, W.; Lu, S.; Liang, J.; He, Z.; Long, H.; Xiong, T.; Sun, H.; He, Q.; Fan, Z.; Zhang, H. Phase Engineering of Nanomaterials for Clean Energy and Catalytic Applications. *Adv. Energy Mater.* **2020**, *10*, 2002019.

(38) Lu, S.; Liang, J.; Long, H.; Li, H.; Zhou, X.; He, Z.; Chen, Y.; Sun, H.; Fan, Z.; Zhang, H. Crystal Phase Control of Gold Nanomaterials by Wet-Chemical Synthesis. *Acc. Chem. Res.* **2020**, *53*, 2106–2118.

(39) Chen, Q. S.; Vidal-Iglesias, F. J.; Solla-Gullón, J.; Sun, S. G.; Feliu, J. M. Role of Surface Defect Sites: From Pt Model Surfaces to Shape-Controlled Nanoparticles. *Chem. Sci.* **2012**, *3*, 136–147.

(40) Rudi, S.; Cui, C.; Gan, L.; Strasser, P. Comparative Study of the Electrocatalytically Active Surface Areas (ECSAs) of Pt Alloy Nanoparticles Evaluated by Hupd and CO-Stripping Voltammetry. *Electrocatalysis* **2014**, *5*, 408–418.

(41) Garrick, T. R.; Moylan, T. E.; Carpenter, M. K.; Kongkanand, A. Editors' Choice—Electrochemically Active Surface Area Measurement of Aged Pt Alloy Catalysts in PEM Fuel Cells by CO Stripping. *J. Electrochem. Soc.* **2017**, *164*, F55–F59.

(42) Stamenkovic, V. R.; Fowler, B.; Mun, B. S.; Wang, G.; Ross, P. N.; Lucas, C. A.; Marković, N. M. Improved Oxygen Reduction Activity on Pt3Ni(111) via Increased Surface Site Availability. *Science* **2007**, *315*, 493–497.

(43) Nagasawa, K.; Takao, S.; Nagamatsu, S. I.; Samjeské, G.; Sekizawa, O.; Kaneko, T.; Higashi, K.; Yamamoto, T.; Uruga, T.; Iwasawa, Y. Surface-Regulated Nano-SnO2/Pt3Co/C Cathode Catalysts for Polymer Electrolyte Fuel Cells Fabricated by a Selective Electrochemical Sn Deposition Method. *J. Am. Chem. Soc.* **2015**, *137*, 12856–12864.

(44) Bunch, J. S.; Van Der Zande, A. M.; Verbridge, S. S.; Frank, I. W.; Tanenbaum, D. M.; Parpia, J. M.; Craighead, H. G.; McEuen, P. L. Electromechanical Resonators from Graphene Sheets. *Science* **2007**, *315*, 490–493.

(45) Tian, X.; Luo, J.; Nan, H.; Zou, H.; Chen, R.; Shu, T.; Li, X.; Li, Y.; Song, H.; Liao, S.; Adzic, R. R. Transition Metal Nitride Coated with Atomic Layers of Pt as a Low-Cost, Highly Stable Electrocatalyst for the Oxygen Reduction Reaction. *J. Am. Chem. Soc.* **2016**, *138*, 1575–1583.

(46) Wang, X.; Kumar, R.; Myers, D. J. Effect of Voltage on Platinum Dissolution Relevance to Polymer Electrolyte Fuel Cells. *Electrochem. Solid-State Lett.* **2006**, *9*, A225.

(47) Lim, C.; Fairhurst, A. R.; Ransom, B. J.; Haering, D.; Stamenkovic, V. R. Role of Transition Metals in Pt Alloy Catalysts for the Oxygen Reduction Reaction. *ACS Catal.* **2023**, *13*, 14874–14893.

(48) Kato, M.; Kimijima, K.; Shibata, M.; Notsu, H.; Ogino, K.; Inokuma, K.; Ohta, N.; Uehara, H.; Uemura, Y.; Oyaizu, N.; Ohba, T.; Takakusagi, S.; Asakura, K.; Yagi, I. Deprotonation of a Dinuclear Copper Complex of 3,5-Diamino-1,2,4-Triazole for High Oxygen Reduction Activity. *Phys. Chem. Chem. Phys.* **2015**, *17*, 8638–8641.

(49) Ravel, B.; Newville, M. ATHENA, ARTEMIS, HEPHAESTUS: Data Analysis for X-Ray Absorption Spectroscopy Using IFEFFIT. In *J. Synchrotron Rad.* **2005**, *12*, 537–541.

SYNOPSIS

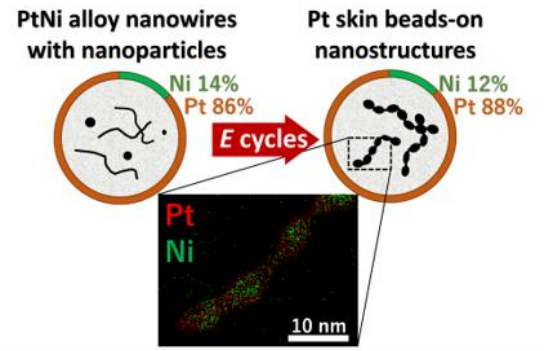
PtNi alloy nanowires with nanoparticles
Pt skin beads-on nanostructures
Ni 14%
Pt 86%
E cycles
Ni 12%
Pt 88%
Pt
Ni
10 nm